Optics and Lasers in Engineering 178 (2024) 108212

Contents lists available at ScienceDirect

Optics and Lasers in Engineering

journal homepage: www.elsevier.com/locate/optlaseng

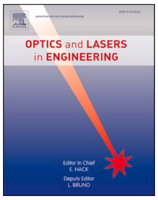

Extended wavefront reconstruction for quadri-wave lateral shearing interferometry

In-Ung Song [a], Jae-Hyuck Choi [a], Hyug-Gyo Rhee [b,c], Hagyong Kihm [a,c], Ho-Soon Yang [a,c,*]

[a] Space Metrology Group, Strategic Technology Research Institute, Korea Research Institute of Standards and Science, 267, Gajeong-ro, Yuseong-gu, Daejeon 34113, Republic of Korea
[b] Length and Dimensional Metrology Group, Division of Physical Metrology, Korea Research Institute of Standards and Science, 267, Gajeong-ro, Yuseong-gu, Daejeon 34113, Republic of Korea
[c] Department of Precision Measurement, University of Science and Technology, 217, Gajeong-ro, Yuseong-gu, Daejeon 34113, Republic of Korea

ARTICLE INFO

Keywords:
Quadri-wave lateral shearing interferometry
Inverse shearing equation
Sub-aperture stitching
Wavefront reconstruction
Large aperture optical testing

ABSTRACT

Quadriwave lateral shearing interferometry (QWLSI) is a well-defined and robust wavefront sensing technique used in various fields such as laser beam qualification, lens or surface testing, bio-imaging, and other advanced optical systems. Despite its strengths, a notable limitation is its inability to measure the edges of the optics because of the non-interfering region in the shearing structure. We present a newly developed method for obtaining extended-aperture wavefront information using QWLSI. The proposed method involves advanced algorithms that analyze the interference patterns from QWLSI using the inverse shearing equation to create four sub-aperture wavefronts up to the edge. These wavefronts are stitched to reconstruct the input wavefront. This technique was successfully applied in testing of a 1.2 m diameter aspheric mirror using QWLSI with infrared laser at 10.6 μm wavelength. The measurement error outside the interferogram area was less than 0.2 μm rms compared to that of the commercially visible interferometer. This error is sufficiently small, supporting the application of this method to the measurement of surfaces during the grinding and early polishing steps. This feature is particularly useful for the large optics, such as mirrors for Giant Magellan Telescope and Extreme Large Telescope.

1. Introduction

Quadriwave lateral shearing interferometry (QWLSI) is a well-defined and robust wavefront sensing technique widely used in various fields, such as laser beam qualification, lens or surface testing, bioimaging, and other advanced optical systems [1–10]. This multi-interference lateral shearing interferometry (LSI) generates four space-shearing wavefronts to obtain interference signals [11]. This unique characteristic offers substantial advantages, such as a wide dynamic range and high robustness to environmental effects in wavefront measurements, as it is a self-referencing interferometer [12–14]. Therefore, it can overcome the narrow dynamic range of commercial interferometers while maintaining good precision.

Recently, Song et al. developed a novel measurement technique called intermediate surface form error metrology (ISFEM) utilizing a commercial QWLSI sensor [15]. The method could assess the surface form error of large-scale optics, specifically those measuring 1.1 m, during grinding fabrication. The approach served as a bridge between rough surface measurements performed with laser trackers and interferometric measurements used for polished surfaces. However, it fails to capture the wavefront error (WFE) in non-interfering regions outside the shearing interferogram. The QWLSI sensor, with a shearing ratio of approximately 2–3 %, leads to data loss spanning approximately 10–15 mm within the aperture for optics of approximately 1 m in size. To address this, Song et al. expanded the physical aperture size, which increased material expenses and weight.

Numerous studies have focused on expanding WFE information in non-interfering areas in LSI. Elster et al. proposed a one-dimensional wavefront reconstruction method based on the difference measurements from two shearing interferograms [16–18]. The algorithm can reconstruct any wavefront exactly up to an arbitrary constant. Okuda et al. developed a modal method using a new Zernike polynomial suitable for a shearing interferogram from a single-directional LSI [19]. Subsequently, Liu et al. improved this method to multidirectional LSI

---

* Corresponding author.
E-mail address: hsy@kriss.re.kr (H.-S. Yang).

https://doi.org/10.1016/j.optlaseng.2024.108212
Received 28 January 2024; Received in revised form 19 March 2024; Accepted 24 March 2024
Available online 4 April 2024
0143-8166/© 2024 Published by Elsevier Ltd.

[20]. Alternatively, Servin et al. presented an inverse shearing method using least-square fitting to solve the ill-posed problem [21,22]. The partial loss in the near-boundary region was constructed from the extracted slopes and integrated wavefronts using an inverse shearing method based on LSI through directional shearing. However, the studies above cannot be directly applied to the reconstruction of WFE using QWLSI sensors. This is because QWLSI sensors create four simultaneously sheared wavefronts, and the interferogram is formed only within the area where these wavefronts overlap.

This study introduces a novel technique for wavefront reconstruction in the non-interfering areas of a QWLSI sensor. This method involves multiple aperture functions and the corresponding inverse shearing equation rooted in the fundamental principles of shearing interferometry [11]. Because QWLSI provides 4-directional slopes from a single interferogram, the proposed method generates four sub-aperture wavefronts stitched to obtain the final extended wavefront. It could be providing the spatially best possible wavefront reconstruction from available interferogram of QWLSI. Section 2 explores the approach behind our proposed technique. Section 3 focuses on the validation of the proposed method using computational simulations. Finally, Section 4 discusses the application of this method in measuring a 1.2-m aspheric mirror, comparing its outcomes with those obtained from standard commercial interferometry.

2. Principle

2.1. Aperture function of the QWLSI

QWLSI consists of an image detector and a unique diffraction grating, known as a modified Hartman mask (MHM) [4,23]. When light enters this system, it diffracts following the 4-directional diffraction vectors, as shown in Fig. 1. The diffraction of MHM can be expressed as 4-directional ±1-order lights approximately. Here, $W_{1,1}$, $W_{-1,1}$, $W_{1,-1}$, and $W_{-1,-1}$ mean the input wavefront (W) sheared in $+x$ or -x directions with $+y$ or -y direction shifts.

The diffracted four sheared wavefronts are tilted with an angle θ_d relative to the optical axis, as follows:

$$W_{m,n} = \left[W\left(x - m\frac{S}{2}, y - n\frac{S}{2}\right) + mT_x + nT_y\right] \cdot A\left(x - m\frac{S}{2}, y - n\frac{S}{2}\right), \quad m,n \in \{-1,1\} \tag{1}$$

where m and n represent the indices of the diffraction order and T_x and T_y denote the tilted wavefronts along the x and y axes, respectively. Variable S corresponds to twice the shearing length of the QWLSI. The $A(x,y)$ is the aperture function has the following properties:

$$A(x,y) = \begin{cases} 1 \text{ if } W(x,y) \text{ is defined} \\ 0 \text{ if } W(x,y) \text{ is not defined} \end{cases}. \tag{2}$$

The variables depend on the diffraction angle (θ_d) and distance of the wavefront propagation from the MHM (z_t), as follows:

$$\begin{aligned} T_x &= x\tan\left(\frac{\theta_d}{\sqrt{2}}\right), \\ T_y &= y\tan\left(\frac{\theta_d}{\sqrt{2}}\right), \\ S &= 2z_t\tan\left(\frac{\theta_d}{\sqrt{2}}\right). \end{aligned} \tag{3}$$

The detection plane is positioned within the Fresnel diffraction region where the four sheared wavefronts overlap to produce an interferogram, as shown in Fig. 2(a). This interferogram can be modulated to generate six sets of phase differences as follows:

$$\begin{aligned} D_1 &= W_{1,1} - W_{-1,1} = \Delta W_x(x, y - S/2) + 2T_x, \\ D_2 &= W_{1,1} - W_{-1,-1} = \Delta W_{x+y}(x,y) + 2T_x + 2T_y, \\ D_3 &= W_{1,1} - W_{1,-1} = \Delta W_y(x - S/2, y) + 2T_y, \\ D_4 &= W_{-1,1} - W_{-1,-1} = \Delta W_y(x + S/2, y) + 2T_y, \\ D_5 &= W_{1,-1} - W_{-1,1} = \Delta W_{x-y}(x,y) + 2T_x - 2T_y, \\ D_6 &= W_{1,-1} - W_{-1,-1} = \Delta W_x(x, y + S/2) + 2T_x. \end{aligned} \tag{4}$$

where ΔW_x, ΔW_y represent the phase differences from shearing along the x- and y-direction, and ΔW_{x+y}, $\Delta W_{x\text{-}y}$ represent the corresponding upper right (↗ ↙) and lower right (↖ ↘) diagonal shearing, respectively. The tilted wavefronts T_x and T_y introduce the carrier frequency of the fringe, and this periodic pattern modulates the phase differences. If I_0 denotes the amplitude of the input wavefront, the modulated interferogram for the QWLSI sensor can be expressed as follows:

$$I(x,y) = \left[\sum_{i=1}^{6} I_0\cos\left(\frac{2\pi}{\lambda}D_i\right)\right] \cdot A_{\text{in}}(x,y), \tag{5}$$

$$A_{\text{in}}(x,y) = \bigcap A\left(x - m\frac{S}{2}, y - n\frac{S}{2}\right), \quad m,n \in \{-1,1\}. \tag{6}$$

Here, A_{in} indicates the aperture function related to the region of the interferogram where the four sheared wavefronts overlap, as indicated by the yellow line in Fig. 2(a). In addition, we define the near boundary region, indicated as A_{out}, which is outside of A_{in} and corresponds to $A \cap (A_{in})^C$ as shown in Fig. 2(b). The wavefront information is reconstructed within A_{in} only, whereas the wavefront in A_{out} is lost.

2.2. Calculation of partial wavefront slope

Let ∇_x and ∇_y be the partial wavefront slopes in the x and y directions and ∇_{x+y} and ∇_{x-y} be the corresponding upper right (↗ ↙) and

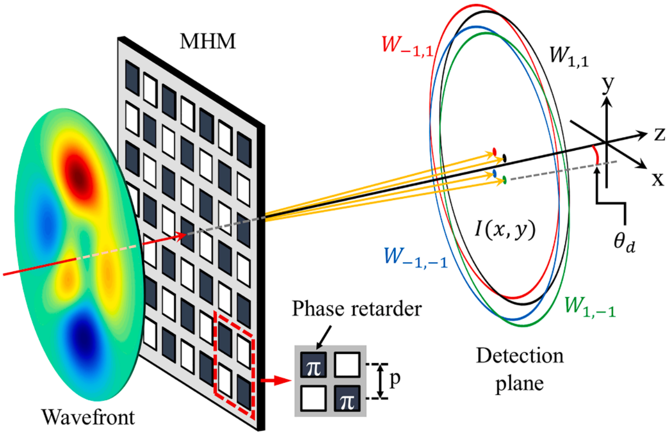

Fig. 1. Schematic layout of the quadriwave lateral shearing interferometry (QWLSI).

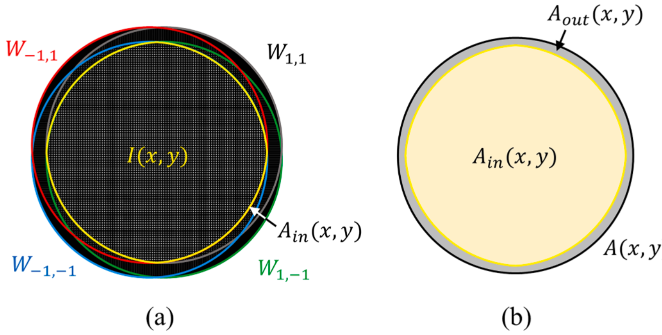

Fig. 2. (a) Diagram of the QWLSI interferogram image in a circular aperture case and (b) area division of input aperture, A(x,y), with A_{in} and A_{out}.

lower right (↖ ↘) diagonal ones. The Fourier method was then used to obtain partial wavefront slopes from the interferogram, as described in Eqs. (7) and (8).

$$\begin{aligned}\nabla_x &= \frac{\lambda}{2\pi}\frac{\arg\left[\mathscr{F}^{-1}(H_{+x})\right]}{S}\cdot A_{\text{in}}(x,y) = \left(\frac{\Delta W_x(x,y-S/2)}{S}+\frac{\Delta W_x(x,y+S/2)}{S}\right)\cdot A_{\text{in}}(x,y),\\ \nabla_y &= \frac{\lambda}{2\pi}\frac{\arg\left[\mathscr{F}^{-1}(H_{+y})\right]}{S}\cdot A_{\text{in}}(x,y) = \left(\frac{\Delta W_y(x-S/2,y)}{S}+\frac{\Delta W_y(x+S/2,y)}{S}\right)\cdot A_{\text{in}}(x,y),\end{aligned} \tag{7}$$

and

$$\begin{aligned}\nabla_{x+y} &= \frac{\lambda}{2\pi}\frac{\arg\left[\mathscr{F}^{-1}(H_{x+y})\right]}{\sqrt{2}S}\cdot A_{\text{in}}(x,y) = \frac{\Delta W_{x+y}(x,y)}{\sqrt{2}S}\cdot A_{\text{in}}(x,y),\\ \nabla_{x-y} &= \frac{\lambda}{2\pi}\frac{\arg\left[\mathscr{F}^{-1}(H_{x-y})\right]}{\sqrt{2}S}\cdot A_{\text{in}}(x,y) = \frac{\Delta W_{x-y}(x,y)}{\sqrt{2}S}\cdot A_{\text{in}}(x,y)\end{aligned} \tag{8}$$

where arg indicates the argument function and $\mathscr{F}^{-1}$ signifies the inverse Fourier transformation. λ is the wavelength of the light, and H_{+x}, H_{+y}, H_{x+y}, and $H_{x\text{-}y}$ are directional harmonics terms. This method separates the harmonic terms of the carrier frequency in the Fourier domain. The regions corresponding to the harmonics of the partial slopes are sampled using spatial windowing. Subsequently, each harmonic term is subjected to an inverse Fourier transformation and divided by the shearing length. The $x + y$ and x - y diagonal partial slopes are uniquely represented by the difference in wavefronts in those directions and a shearing length of $\sqrt{2}S$, whereas the partial slopes in the x- and y-directions are entangled. Therefore, we focus on obtaining the partial wavefront slopes in the two diagonal directions instead of in the x- and y-directions.

We reconstruct wavefront W_r by integrating ∇_{x+y} and ∇_{x-y} obtained from Eq. (8) using the carrier wave or the modified Southwell Zonal method [24,25]. W_r is constrained within A_{in} or is expressed using Eq. (9).

$$W_r \approx W\cdot A_{\text{in}} \tag{9}$$

2.3. Inverse shearing equation

Let $(x_1,\ y_1)$ be the element of A_{out}, which satisfies the following:

$$x_0 = x_1 - \frac{S}{2},\quad y_0 = y_1 - \frac{S}{2},\quad (x_0,y_0)\in A_{\text{in}} \tag{10}$$

According to Eq. (4), the wavefront phase difference at a point in the first quadrant of A_{in} is

$$\begin{aligned}\Delta W_{x+y}(x_0,y_0) &= W_{1,1}(x_0,y_0) - W_{-1,-1}(x_0,y_0)\\ &= W\left(x_0-\frac{S}{2},y_0-\frac{S}{2}\right) - W\left(x_0+\frac{S}{2},y_0+\frac{S}{2}\right).\end{aligned} \tag{11}$$

Then, the wavefront at $(x_1,\ y_1)$ can be calculated as

$$W(x_1,y_1) = W(x_1-S,y_1-S) - \Delta W_{x+y}\left(x_1-\frac{S}{2},y_1-\frac{S}{2}\right) \tag{12}$$

As $(x_1 - S,\ y_1 - S)$ and $(x_1 - S/2,\ y_1 - S/2)$ are elements of A_{in}, Eqs. (12) becomes

$$W(x_1,y_1) \approx W_r(x_1-S,y_1-S) - \Delta W_{x+y}\left(x_1-\frac{S}{2},y_1-\frac{S}{2}\right) \tag{13}$$

Thus, we can obtain the wavefront at any points in the first quadrant of A_{out} using the known information of reconstructed wavefront, W_r, and the wavefront phase difference, ΔW_{x+y}, at any points in the first quadrant of A_{in}. Hence, in this paper, Eq. (13) is referred to as the "inverse shearing equation".

Next, we define a new subaperture $A_{sub}^{1,1}$, with respect to Eq. (13), as follows:

$$A_{sub}^{1,1}(x,y) = \left[A_{\text{in}}(x-S,y-S)\cap A_{\text{in}}\left(x-\frac{S}{2},y-\frac{S}{2}\right)\right] \tag{14}$$

where index (1,1) is the sheared area in the same direction as $W_{1,1}$. Fig. 3 shows an example diagram explaining the subaperture $A_{sub}^{1,1}$, from the inverse shearing equation for the first quadrant subaperture wavefront. Similarly, we can calculate the wavefront at a point in any quadrant of the input aperture A or

$$W_{sub}^{m,n}(x,y) = \left[W_r(x-mS,y-nS) - m\Delta W_{x\pm y}\left(x-m\frac{S}{2},y-n\frac{S}{2}\right)\right]\cdot A_{sub}^{m,n}(x,y),\quad m,n \in\{1,-1\} \tag{15}$$

where $W_{sub}^{m,n}$ indicates the wavefront of the subaperture defined by the four different quadrants of $A_{sub}^{m,n}$ as follows:

$$A_{sub}^{m,n}(x,y) = \left[A_{\text{in}}(x-mS,y-nS)\cap A_{\text{in}}\left(x-m\frac{S}{2},y-n\frac{S}{2}\right)\right],\quad m,n\in\{1,-1\} \tag{16}$$

We then reconstruct the extended wavefront (W_{ext}) by stitching the four sub-aperture wavefronts, as shown in Fig. 4 [26–29]. The total stitched area is calculated as follows:

$$W_{ext} \approx W\cdot A_{ext}(x,y), \tag{17}$$

$$A_{ext} = \bigcup A_{sub}^{m,n}(x,y),\quad m,n\in\{1,-1\}. \tag{18}$$

At this stage, the aperture function A_{ext} is very close to A but not the same because we use four diagonal shearing wavefronts, as shown in Fig. 4. We calculated the amount of information lost in our method, depending on the shearing ratio. Fig. 5 shows the ratio of the reconstructed area to the input aperture as the shearing ratio changes from 0 to 0.1. The blue and red lines represent the results with the proposed method and original QWLSI, respectively. Our method retains a reconstruction ratio of more than 99.9 %, whereas the original QWLSI drops to approximately 77.5 % at the 0.1 shearing ratio. This implies that most of the input wavefront information can be obtained, and a small amount of lost information can be recovered using interpolation without significant accuracy degradation.

3. Simulation

Computational simulations were conducted to validate the proposed method. We created a simulated input wavefront (W_{sim}) using MATLAB®'s peaks function, as depicted in Fig. 6(a). This wavefront was scaled to achieve a peak-to-valley measurement of 25.85 µm and rms of 4.18 µm, which is sufficiently large for detection by a QWLSI sensor. The wavefront image was designed with a diameter of 7.5 mm and a central hole measuring 1.1 mm. Fig. 6(b) shows the simulated interferogram (I_{sim}) obtained using Eqs. (2)–(5). The QWLSI wavefront sensor

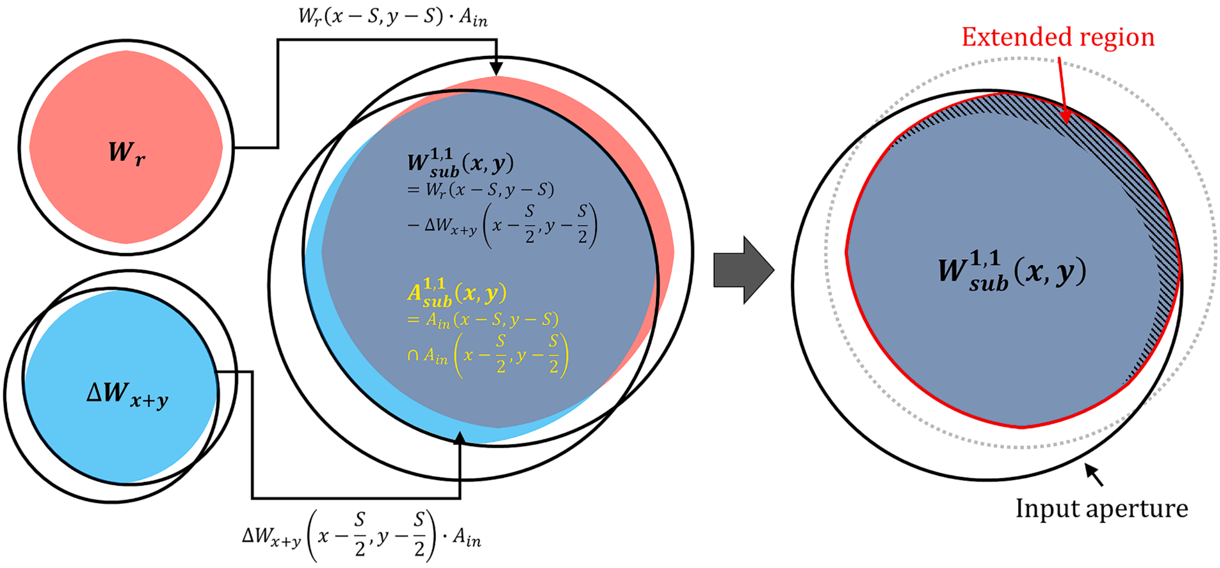

Fig. 3. Diagram explaining obtaining $W_{sub}^{1,1}$ using the inverse shearing equation.

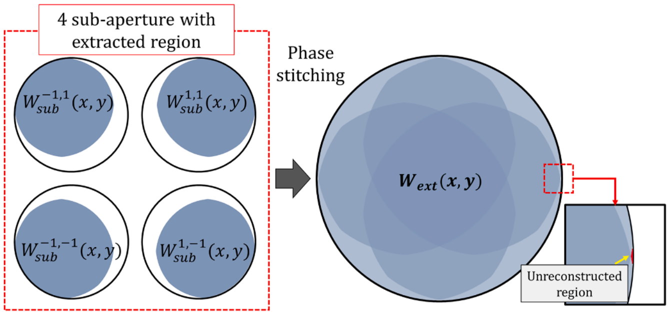

Fig. 4. Four sub-apertures generated by the inverse shearing equation and their stitching process to obtain input wavefront.

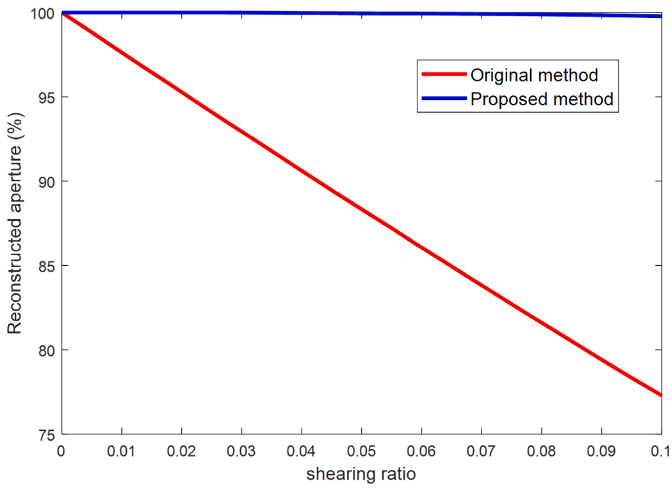

Fig. 5. Comparison of the area ratio of the reconstructed apertures from the original QWSLI sensor (red line) and our proposed method (blue line) with respect to the shearing ratio (0–0.1).

specifications are outlined in Table 1. I_{sim} was then displayed within A_{in}, which has a diameter of approximately 97 % of the total aperture area.

We derive the reconstructed wavefront, W_r, depicted in Fig. 7(a), using a modified zonal integration method applied to I_{sim}, with adjustments for the shearing length. Consequently, W_r is restricted to the A_{in} area. The black line represents the size of the initial wavefront, W_{sim}. Fig. 7(b) presents the extended wavefront, W_{ext}, which was generated by merging the four sub-aperture wavefronts using Eq. (14). In this calculation, the phase translation of each sub-aperture adopted the triangulation-based cubic method. The stitching algorithm used the least square method by controlling piston and tilt of Zernike polynomials [27]. Fig. 7(c) shows the miss-match map of the stitching algorithm. Fig. 7(d) illustrates the discrepancy between W_{sim} and W_{ext}, which is a 0.13 µm *rms* or 3 % of the initial wavefront. This small deviation suggests that the QWLSI sensor is suitable for surface-error measurements during grinding and early polishing steps. This error includes both systematic errors in the QWLSI hardware and the post-processing error of

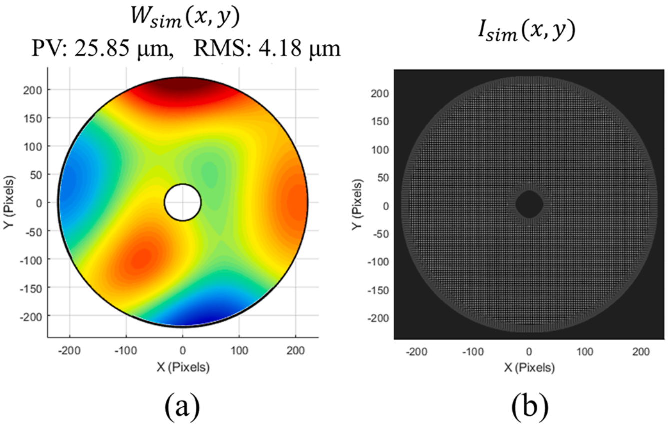

(a) (b)

Fig. 6. (a) Simulated wavefront and (b) theoretical interferogram.

Table 1
Specification of QWLSI wavefront sensor.

Simulation parameters	Value
Wavelength (λ)	10.6 µm
Entrance pupil diameter	8.16 mm
Grating period of the MHM (p)	68 µm
Distance between MHM and detector (z_t)	1.5 mm
Number of calculation pixels	480 × 480 pixels
Shearing length (S)	235 µm

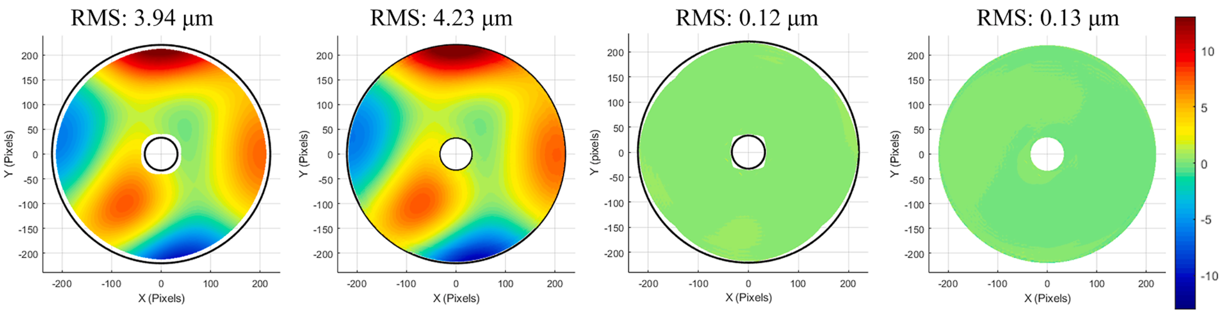

(a) (b) (c) (d)

Fig. 7. (a) Reconstructed wavefront (W_r), (b) extended wavefront (W_{ext}), (c) miss-match map of the stitching, and (d) residual map between W_{sim} of Fig. 6(a) and W_{ext}.

our proposed method. In this paper, we focus on the post-processing technique of which error could stem from factors such as Fourier demodulation, zonal integration, or image translation within a finite matrix. Therefore, these aspects can be further improved through additional research. For example, if we use a higher number of sampling points, the interpolation error can be reduced, which can lead to more accurate sub-aperture positioning and improved stitched results for the extended wavefront.

4. Experiment

We employed an ISFEM instrument integrated with a QWLSI wavefront sensor (SID4-DWIR, Phasics Co.) to measure a ellipsoid mirror with a 1.2-m diameter[15]. This sensor comprises a 640 × 480 pixels bolometer and operates with a 10.6 μm wavelength laser. In our previous study [15], the measurement achieved an accuracy of approximately 75 nm rms, with the specifications presented in Table 1.

Developed initially for assessing mirror surfaces during the grinding step, our setup, depicted in Fig. 8, incorporates a null system for generating an aspheric wavefront corresponding to the ellipsoid mirror, with a 3.8 m radius of curvature and −0.987 conic constant. The null system was meticulously designed and manufactured, integrating alignment datums to guarantee the reference wavefront of the aspheric surface. In this step, ISFEM was applied to measure the surface during the early polishing step because the measurement result needed to be compared to that of commercial interferometry.

We obtained an interferogram from the QWLSI wavefront sensor used in the ISFEM, as shown in Fig. 9(a). In this testing, we ensured a signal-to-noise ratio (SNR) of the interferogram above 20 dB to mitigate the influence of noise [15]. The shearing ratio of QWLSI is approximately 3 %, which corresponds to the wavefront loss width of 17.5 mm for 1.2 m diameter, as demonstrated in Fig. 9(b).

Fig. 10(a) shows the reconstructed surface form error obtained using the original method. Only the interferogram area could be reconstructed. Fig. 10(b) shows the extended surface form error obtained using our proposed method. The area of A_{out} was well filled to reproduce the input wavefront, which is close to the result of a commercial interferometer (PhaseCam 5030 from 4D Technology Co.) with a computer-generated hologram (CGH), as shown in Fig. 10(c). Fig. 10(d) displays the miss-match map with the stitching error of 0.12 μm rms.

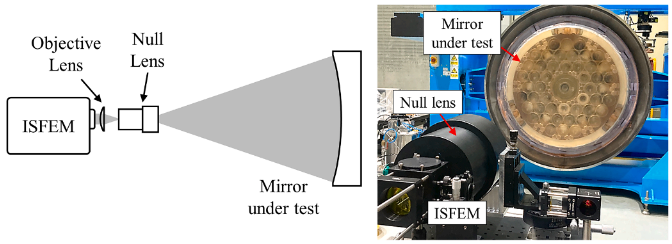

(a) (b)

Fig. 8. (a) Schematic of the ellipsoid mirror surface test using intermediate surface form error metrology (ISFEM) and (b) a photograph of the test setup.

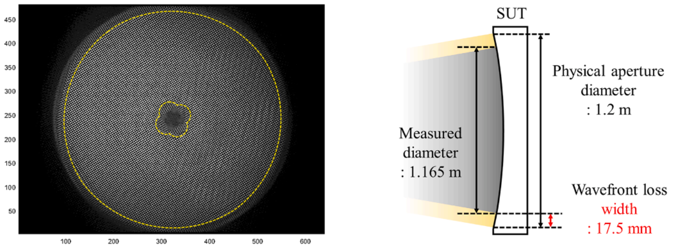

(a) (b)

Fig. 9. (a) Interferogram of the 1.2 m ellipsoid mirror from QWLSI sensor (Yellow dot line) and (b) schematic of the wavefront loss width.

To assess the accuracy of the reconstructed extended wavefront, the surface profiles at $r = 594$ mm in the A_{out} region are compared in Figs. 10 (b) and (c), as illustrated in Fig. 11. Both profiles exhibit similar peaks and troughs, aligning closely with a peak-to-valley measurement of 0.77 and 0.16 μm rms. This level of difference is on the order of the measurement accuracy of the ISFEM, as reported in our earlier paper [15]. Moreover, this is comparable to the simulated results presented in Fig. 7 (c). Therefore, this error margin can be attributed to the measurement accuracy of the ISFEM and computational errors, such as those arising from Fourier demodulation, zonal integration, or image translation within a limited matrix. This analysis could offer insight into the scale of measurement errors. However, adopting the absolute evaluation using closure relations could further improve confidence in QWLSI itself, which will be carried out in near future [30]. In summary, these findings confirm the effectiveness of our method in reconstructing the wavefronts beyond the QWLSI interferogram region.

5. Conclusions

This paper presents the effectiveness of a newly developed method for extended wavefront reconstruction in QWLSI. The method involves advanced algorithms that analyze the interference patterns from QWLSI using the inverse shearing equation to create four subaperture wavefronts. These wavefronts are stitched to reconstruct the input wavefront. This technique was successfully applied in testing a 1.2 m aspheric mirror. The measurement error outside the shearing interferogram was less than 0.2 μm rms compared to that of a commercially visible interferometer. The small error allowed us to apply this method for surface measurements during grinding and early polishing. Moreover, it opens opportunities for using QWLSI in segmented mirror testing, such as Giant Magellan Telescope mirrors, requiring stringent specifications for

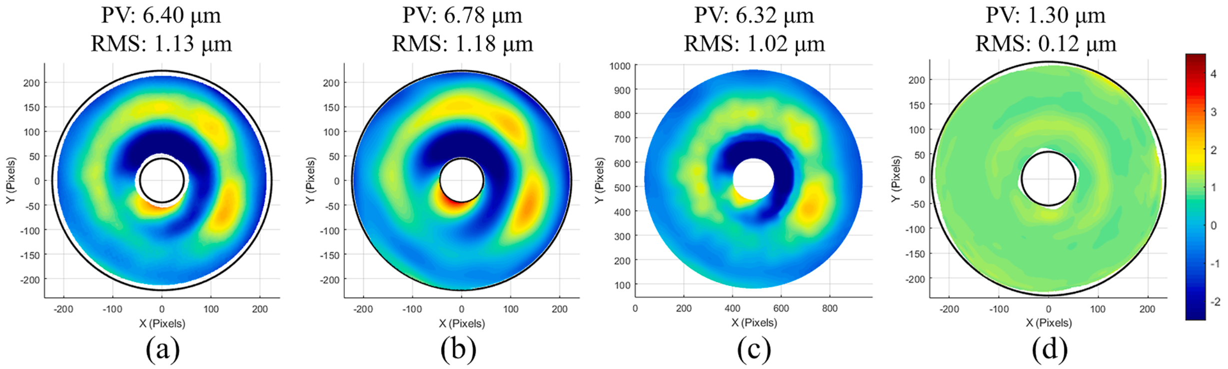

Fig. 10. Surface form errors measured by (a) ISFEM with the original method, (b) proposed method, (c) commercial interferometer, and (d) miss-match map of the stitching.

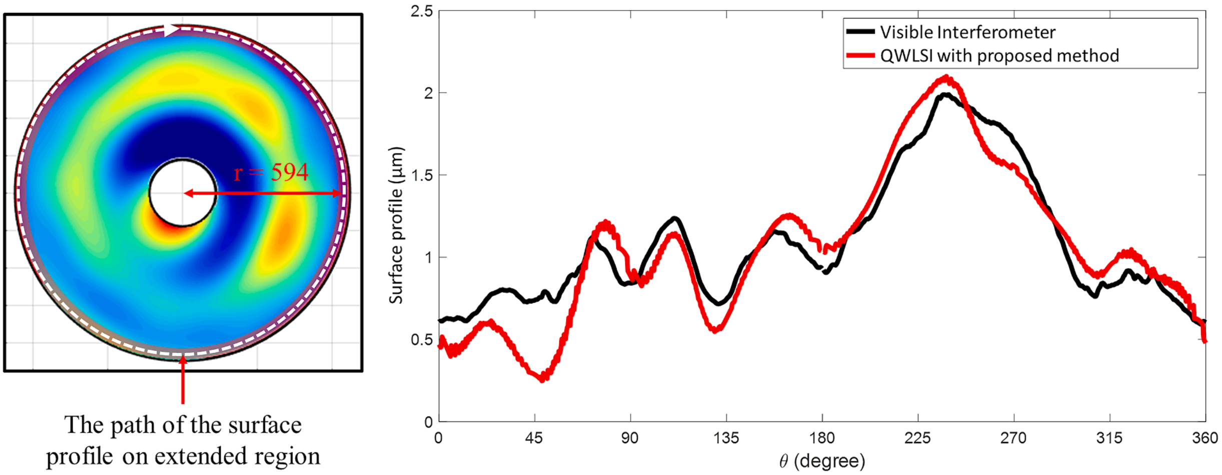

Fig. 11. Comparison of surface profiles between the visible interferometer and QWLSI results (following the path on the extended region at $r = 594$ mm).

surface form errors near the aperture boundary.

One drawback of our method is its weakness in obtaining the full-aperture for the special aperture shape, such as a hexagonal shape of James Webb Space Telescope (JWST), because the hexagonal vertices coincide with the unreconstructed region. This problem needs to be tackled in the future. Fortunately, this issue may be addressed by employing other multi-LSI techniques, such as three-wave lateral shearing interferometry (TWLSI) [31], in conjunction with our method. This approach could prove beneficial in enhancing the throughput of large optics manufacturing with hexagonal apertures.

CRediT authorship contribution statement

In-Ung Song: Writing – original draft, Software, Methodology, Formal analysis, Conceptualization, Investigation. **Jae-Hyuck Choi:** Data curation, Validation, Writing – review & editing. **Hyug-Gyo Rhee:** Software, Formal analysis. **Hagyong Kihm:** Funding acquisition, Resources. **Ho-Soon Yang:** Writing – review & editing, Supervision, Project administration.

Declaration of competing interest

The authors declare the following financial interests/personal relationships which may be considered as potential competing interests:

In-Ung Song has patent pending to Korea Research Institute of Standards and Science (KRISS). If there are other authors, they declare that they have no known competing financial interests or personal relationships that could have appeared to influence the work reported in this paper.

Acknowledgments

This research was supported by the National R&D Program through the National Research Foundation of Korea (NRF), funded by the Ministry of Science and ICT grant 2021M3H4A3A01055840.

The authors greatly appreciate the valuable discussions by Dr. Jae-Cheul Lee regarding implementing theoretical definition.

References

[1] Han Z-G, Meng L-Q, Huang Z-Q, Shen H, Chen L, Zhu R-H. Determination of the laser beam quality factor (M2) by stitching quadriwave lateral shearing interferograms with different exposures. Appl Opt 2017;56:7596–603. https://doi.org/10.1364/AO.56.007596.

[2] Meng L, Liu Y, Han Z, Shen H, Chen L, Zhu R. Analysis of laser M2 determination in a quadriwave lateral shearing interferometer with CCD vertical blooming. Opt Commun 2019;433:183–9. https://doi.org/10.1016/j.optcom.2018.10.003.

[3] Boucher W, Delage P, Wattellier B. Aspherical surface measurement using quadri-wave lateral shearing interferometry. editors. In: Lehmann PH, Osten W, Gastinger K, editors. Optical measurement systems for industrial inspection VII, vol. 8082. SPIE; 2011. 80821E. https://doi.org/10.1117/12.895005.

[4] Velghe S, Haïdar R, Guérineau N, Tauvy M, Rommeluère S, Thétas S, et al. In situoptical testing of infrared lenses for high-performance cameras. Appl Opt 2006; 45:5903–9. https://doi.org/10.1364/AO.45.005903.

[5] Aknoun S, Bon P, Savatier J, Wattellier B, Monneret S. Quantitative retardance imaging of biological samples using quadriwave lateral shearing interferometry. Opt Express 2015;23:16383. https://doi.org/10.1364/OE.23.016383.

[6] Bon P, Maucort G, Wattellier B, Monneret S. Quadriwave lateral shearing interferometry for quantitative phase microscopy of living cells. Opt Express 2009; 17:13080. https://doi.org/10.1364/oe.17.013080.

[7] Baffou G. Quantitative phase microscopy using quadriwave lateral shearing interferometry (QLSI): principle, terminology, algorithm and grating shadow

description. J Phys D Appl Phys 2021;54:294002. https://doi.org/10.1088/1361-6463/abfbf9.
[8] Mousset S, Rouyer C, Marre G, Blanchot N, Montant S, Wattellier B. Piston measurement by quadriwave lateral shearing interferometry. Opt Lett 2006;31:2634–6. https://doi.org/10.1364/OL.31.002634.
[9] Bellanger C, Toulon B, Primot J, Lombard L, Bourderionnet J, Brignon A. Collective phase measurement of an array of fiber lasers by quadriwave lateral shearing interferometry for coherent beam combining. Opt Lett 2010;35:3931–3. https://doi.org/10.1364/OL.35.003931.
[10] Khadir S, Andrén D, Verre R, Song Q, Monneret S, Genevet P, et al. Metasurface optical characterization using quadriwave lateral shearing interferometry. ACS Photonics 2021;8:603–13. https://doi.org/10.1021/acsphotonics.0c01707.
[11] Malacara D. Optical shop testing. vol. 59. John Wiley & Sons; 2007.
[12] Chanteloup JC. Multiple-wave lateral shearing interferometry for wave-front sensing. Appl Opt 2005;44:1559–71. https://doi.org/10.1364/AO.44.001559.
[13] Velghe S, Primot J, Guérineau N, Cohen M, Wattellier B. Visible and infrared wave-front metrology by quadri-wave lateral shearing interferometry. editors. In: Duparré A, Geyl R, Wang L, editors. Optical fabrication, testing, and metrology II, vol. 5965. SPIE; 2005. p. 331–8. https://doi.org/10.1117/12.626248.
[14] Velghe S, Primot J, Guérineau N, Haïdar R, Demoustier S, Cohen M, et al. Advanced wave-front sensing by quadri-wave lateral shearing interferometry. editors. In: Creath K, Schmit J, editors. Interferometry XIII: techniques and analysis, vol. 6292. SPIE; 2006. p. 117–29. https://doi.org/10.1117/12.681533.
[15] Song I-U, Yang H-S, Kim G, Kim S-W. Surface form error measurement for rough surfaces using an infrared lateral shearing interferometry. Opt Lasers Eng 2022;152:106947. https://doi.org/10.1016/j.optlaseng.2022.106947.
[16] Elster C, Weingärtner I. Solution to the shearing problem. Appl Opt 1999;38:5024–31. https://doi.org/10.1364/AO.38.005024.
[17] Elster C, Weingärtner I. Exact wave-front reconstruction from two lateral shearing interferograms. J Opt Soc Am A 1999;16:2281–5. https://doi.org/10.1364/JOSAA.16.002281.
[18] Falldorf C, Heimbach Y, von Kopylow C, Jüptner W. Efficient reconstruction of spatially limited phase distributions from their sheared representation. Appl Opt 2007;46:5038–43. https://doi.org/10.1364/AO.46.005038.
[19] Okuda S, Nomura T, Kamiya K, Miyashiro H, Yoshikawa K, Tashiro H. High-precision analysis of a lateral shearing interferogram by use of the integration method and polynomials. Appl Opt 2000;39:5179–86. https://doi.org/10.1364/AO.39.005179.
[20] Liu K, Wang J, Wang H, Li Y. Wavefront reconstruction for multi-lateral shearing interferometry using difference Zernike polynomials fitting. Opt Lasers Eng 2018;106:75–81. https://doi.org/10.1016/j.optlaseng.2018.02.011.
[21] Servin M, Malacara D, Marroquin JL. Wave-front recovery from two orthogonal sheared interferograms. Appl Opt 1996;35:4343–8. https://doi.org/10.1364/AO.35.004343.
[22] Servin M, Cywiak M, Dávila A. Lateral shearing interferometry: theoretical limits with practical consequences. Opt Express 2007;15:17805–18. https://doi.org/10.1364/OE.15.017805.
[23] Primot J, Guérineau N. Extended Hartmann test based on the pseudoguiding property of a Hartmann mask completed by a phase chessboard. Appl Opt 2000;39:5715. https://doi.org/10.1364/ao.39.005715.
[24] Southwell WH. Wave-front estimation from wave-front slope measurements. J Opt Soc Am 1980;70:998–1006. https://doi.org/10.1364/JOSA.70.000998.
[25] Nguyen V-H-L, Rhee H-G, Ghim Y-S. Improved iterative method for wavefront reconstruction from derivatives in grid geometry. Curr Opt Photon 2022;6:1–9.
[26] Otsubo M, Okada K, Tsujiuchi J. Measurement of large plane surface shapes by connecting small-aperture interferograms. Opt Eng 1994;33:608–13. https://doi.org/10.1117/12.152248.
[27] Zhao C, Burge JH. Stitching of off-axis sub-aperture null measurements of an aspheric surface. editors. In: Schmit J, Creath K, Towers CE, editors. Interferometry XIV: techniques and analysis, vol. 7063. SPIE; 2008, 706316. https://doi.org/10.1117/12.795094.
[28] Chen S, Zhao C, Dai Y, Li S. Stitching algorithm for subaperture test of convex aspheres with a test plate. Opt Laser Technol 2013;49:307–15. https://doi.org/10.1016/j.optlastec.2013.01.023.
[29] Zhao C, Sprowl RA, Bray M, Burge JH. Figure measurement of a large optical flat with a Fizeau interferometer and stitching technique. editors. In: Novak EL, Osten W, Gorecki C, editors. Interferometry XIII: applications, vol. 6293. SPIE; 2006. p. 160–8. https://doi.org/10.1117/12.681234.
[30] Stolidi A, Giakoumakis G, Primot J, Jarnac A, Tisseur D. Confidence map tool for gradient-based X-ray phase contrast imaging. Opt Express 2022;30:4302–11. https://doi.org/10.1364/OE.438876.
[31] Primot J. Three-wave lateral shearing interferometer. Appl Opt 1993;32:6242–9. https://doi.org/10.1364/AO.32.006242.